Quaternary Science Reviews 95 (2014) 80–94

Contents lists available at ScienceDirect

Quaternary Science Reviews

journal homepage: www.elsevier.com/locate/quascirev

Why so few? Landslides triggered by the 2002 Denali earthquake, Alaska

Tolga Gorum [a,b,*], Oliver Korup [c], Cees J. van Westen [a], Mark van der Meijde [a], Chong Xu [d], Freek D. van der Meer [a]

[a] Faculty of Geo-Information Science and Earth Observation (ITC), University of Twente, 7500 AE Enschede, P.O. Box 217, The Netherlands
[b] Natural Sciences Research Center, Yildiz Technical University, Esenler, 34220 Istanbul, Turkey
[c] Institute of Earth and Environmental Sciences, University of Potsdam, D-14476 Potsdam, Germany
[d] Key Laboratory of Active Tectonics and Volcanoes, Institute of Geology, Chinese Earthquake Administration, Beijing 100029, People's Republic of China

ARTICLE INFO

Article history:
Received 4 January 2014
Received in revised form
26 April 2014
Accepted 30 April 2014
Available online

Keywords:
Earthquake
Landslide
Glacial
Sediment cascade
Denali
Alaska

ABSTRACT

The 2002 M_w 7.9 Denali Fault earthquake, Alaska, provides an unparalleled opportunity to investigate in quantitative detail the regional hillslope mass-wasting response to strong seismic shaking in glacierized terrain. We present the first detailed inventory of ~1580 coseismic slope failures, out of which some 20% occurred above large valley glaciers, based on mapping from multi-temporal remote sensing data. We find that the Denali earthquake produced at least one order of magnitude fewer landslides in a much narrower corridor along the fault ruptures than empirical predictions for an M ~8 earthquake would suggest, despite the availability of sufficiently steep and dissected mountainous topography prone to frequent slope failure. In order to explore potential controls on the reduced extent of regional coseismic landsliding we compare our data with inventories that we compiled for two recent earthquakes in periglacial and formerly glaciated terrain, i.e. at Yushu, Tibet (M_w 6.9, 2010), and Aysén Fjord, Chile (2007 M_w 6.2). Fault movement during these events was, similarly to that of the Denali earthquake, dominated by strike-slip offsets along near-vertical faults. Our comparison returns very similar coseismic landslide patterns that are consistent with the idea that fault type, geometry, and dynamic rupture process rather than widespread glacier cover were among the first-order controls on regional hillslope erosional response in these earthquakes. We conclude that estimating the amount of coseismic hillslope sediment input to the sediment cascade from earthquake magnitude alone remains highly problematic, particularly if glacierized terrain is involved.

1. Introduction

Glaciated mountain belts offer rich and diverse archives of Quaternary environmental change. Particularly the reconstruction of the extent and timing of glacial fluctuations from diagnostic sediments and landforms has had a strong research tradition with many vital implications for independently constraining paleoclimatic time series. Even so a growing number of studies that highlight the potential for confusing glacial moraines as classic paleoclimatic proxies with deposits from catastrophic landslides—and vice versa—has spurred fresh enquiries into the role of controls other than climatic on glacier dynamics (Hewitt, 1999; Tovar et al., 2008; Reznichenko et al., 2012). The same goes for detailed studies of the interactions between glacial and hillslope processes such as the formation of catastrophic rock-ice avalanches (Evans et al., 2009; Fischer et al., 2013) or the effect of supraglacial rock-avalanche debris on glacial advances or stagnation (Hewitt, 2009; Shulmeister et al., 2009; Vacco et al., 2010; Shugar et al., 2012; Menounos et al., 2013) that may eventually compromise interpretations solely devoted to unraveling paleoclimatic fluctuations. In this context, the study of earthquake impacts in glaciated terrain offers particularly fascinating insights into the manifold feedbacks at the interface between seismology, glaciology, and Quaternary geomorphology. For one, widespread deglaciation is known to trigger crustal response and glacioisostatic rebound, which in turn may prompt fault (re-)activation in tectonically active mountain belts (Sauber and Molnia, 2004; McColl et al., 2012). Also,

* Corresponding author. Natural Sciences Research Center, Yildiz Technical University, Esenler, 34220 Istanbul, Turkey. Tel.: +31 (0) 53 487 4504.
E-mail addresses: tgorum@yildiz.edu.tr, tgorum@gmail.com (T. Gorum).

http://dx.doi.org/10.1016/j.quascirev.2014.04.032

strong earthquakes provide sufficient ground acceleration to cause regional hillslope mass-wasting even in glaciated areas where most of the precipitation is falling as snow, and heavy rainfall is a less likely alternative trigger of widespread rock and ice instability (van der Woerd et al., 2004). Little is known, for example, about whether and how thick ice cover contributes to buffering incoming seismic waves and therefore the earthquake-triggered release of hillslope debris into the glacial sediment cascade. Uhlmann et al. (2013) estimated that nearly three quarter of the high contemporary supraglacial sediment flux on glaciers in the Chugach Mountains, south-central Alaska, may have originated from earthquake shaking. However, McColl et al. (2012) argued that thick ice caps can repress coseismic shaking and reduce landslide volumes, and also that with less ice cover (~50% of local topographic relief buried) this effect becomes minute. Refining such estimates requires comprehensive sediment budgets in glaciated environments. Studying the direct mass-wasting impacts of historic earthquakes is one of the avenues to unravel better the relevance of episodic seismic disturbances in glaciated mountain belts.

The M_w 7.9 Denali Fault earthquake struck south-central Alaska and the Alaska Range at 13:12 local time (22:12 UTC) on November 3, 2002. It was one of the largest earthquakes in U.S. history, rupturing three major faults over a distance of 340 km in 100 s. The earthquake hypocenter was at a depth of 5 km on an ENE striking plane (18.44° N, 72.57° W, U.S. Geological Survey, 2002; Fig. 1). The Alaska Earthquake Information Center linked the location and mechanism to the rupture of multiple faults, and mainly the right-lateral Denali Fault, which is part of a system of active intra-continental strike-slip faults accommodating contemporary slip rates of 8–9 mm yr^{-1} along the North American–Pacific plate boundary.

Inversion of strong-motion data, GPS data, and surface offset measurements revealed that the earthquake consisted of three sub-events standing out as areas with above-average coseismic slip (Hreinsdottir et al., 2006; Frankel, 2004; Ozacar and Beck, 2004; Fig. 1). Seismic shaking originated from thrust motion on the north-dipping Susitna Glacier Fault near the epicenter, with an average dip slip of 4 m (Haeussler et al., 2004). The subsequent M_w 7.3 sub-event ~60–100 km E of the epicenter entailed a 226-km rupture of the Denali Fault with right-lateral slip at the surface averaging 4.5–5.1 m. A maximum offset of 8.8 m was recorded ~40 km W of the Denali-Totschunda Fault branch, where the third M_w 7.6 sub-event originated (Eberhart-Phillips et al., 2003; Frankel, 2004; Haeussler et al., 2004; Hreinsdottir et al., 2006). Fault rupture propagated for another 66 km along the Totschunda Fault, where right-lateral surface offsets averaged 1.7 m (Eberhart-Phillips et al., 2003; Haeussler et al., 2004).

About 1000 landslides were attributed to the Denali earthquake based on an aerial reconnaissance shortly after, including seven rock avalanches with a total volume of nearly 80 × 10^6 m^3 that traveled onto the Black Rapids, McGinnis, and West Fork Glaciers (Harp et al., 2003; Jibson et al., 2004, 2006). However, no substantially complete landslide inventories for this earthquake were done. This earthquake provides exceptional opportunities to

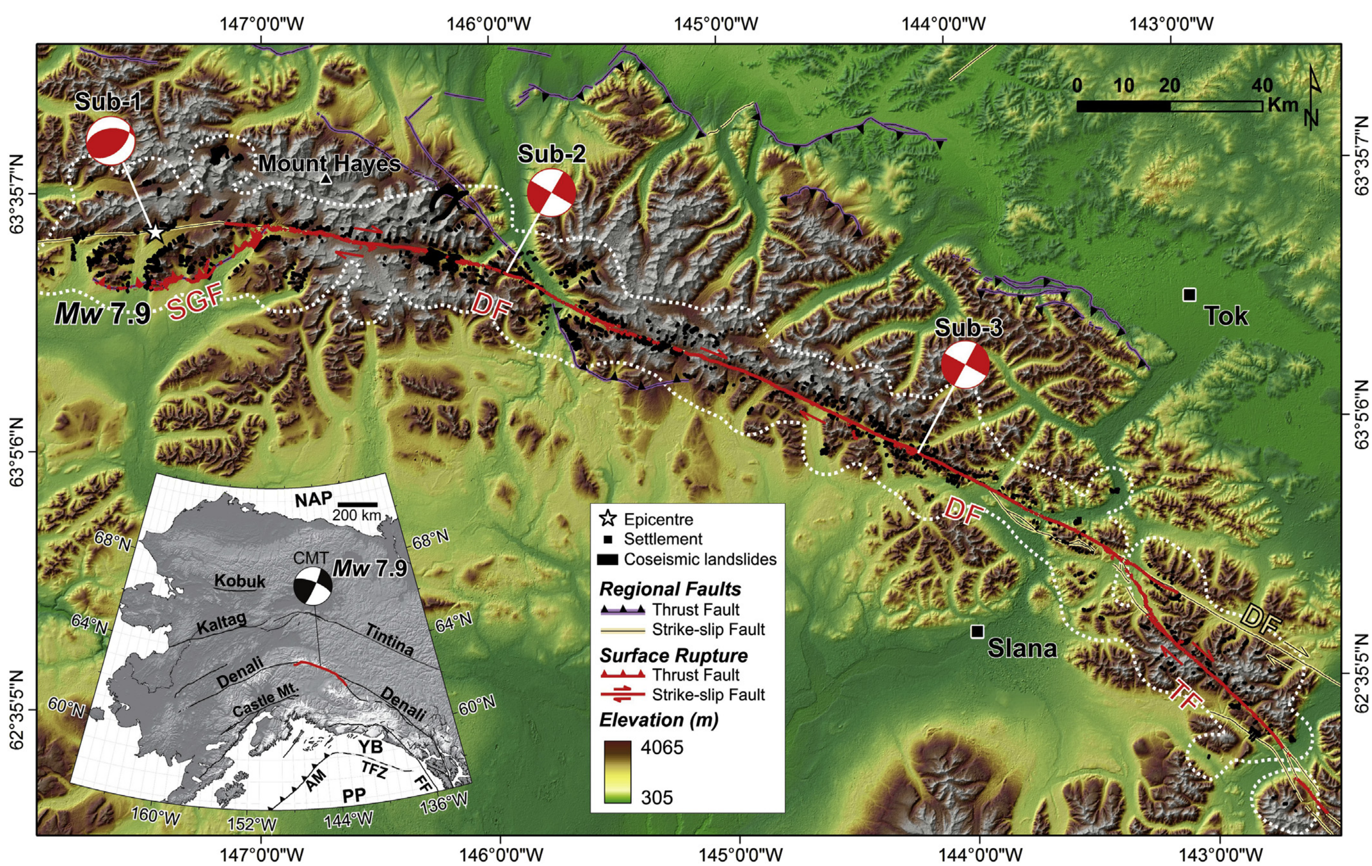

Fig. 1. Distribution of ~1580 landslides triggered by the 2002 Denali Fault earthquake, and tectonic setting of the study area. Red lines are surface traces of coseismic rupture (Haeussler, 2009); beach balls show focal mechanism of the first-motion solution (Sub-1), and the two largest sub-events from waveform inversion (Sub-2, and Sub-3; Eberhart-Phillips et al., 2003). Dashed white lines delimit coseismic landslide densities >0.01 km^{-2}. Inset shows major tectonic boundaries between North American Plate (NAP), Pacific Plate (PP), and Yakutat Block (YB); focal mechanism is Harvard CMT solution; AM: Alaska megathrust, FF: Fairweather Fault, TFZ: Transition fault zone between Alaska and Yukon terranes. (For interpretation of the references to color in this figure legend, the reader is referred to the web version of this article.)

investigate in detail the geomorphic hillslope response by mass wasting in glacierized terrain.

To this end, we explore seismological, lithologic, and topographic controls on the spatial pattern and size distribution of landslides triggered by the 2002 Denali earthquake. Our objectives are (1) to decipher from a substantially complete inventory of ~1580 coseismic landslides the roles of dynamic rupture process, fault geometry, rupture directivity, glacier cover, local topographic relief, and hillslope steepness in modulating the regional pattern of coseismic mass-wasting response; and (2) to compare these results with patterns from other coseismic landslide inventories obtained following recent earthquakes on strike-slip faults in periglacial and postglacial mountainous terrain of Tibet and Chile.

2. Study area

We focus on the main epicentral area of the 2002 Denali earthquake in the central and eastern Alaska Range (Fig. 1), a 950-km long mountain belt that is 70–200 km wide. The Alaska Range is the result of a collision of an island arc with the North American continental margin that has gradually deformed since the Late Mesozoic (Ridgway et al., 2002; Matmon et al., 2006). The range rises from low foothills at <800 m a.s.l. to the highest peak (4150 m a.s.l.) in the central part, sustaining a local relief of >3300 m. This topographic barrier enhances the contrast between cold continental and mild maritime climate on the northern and southern range flanks, respectively (Capps, 1940). The rugged bedrock landscape features jagged peaks, serrated ridges, and trough valleys that indicate widespread glacier cover during the Last Glacial Maximum around 20 ka, though ice extent was largely limited on the northern slopes of the range (Dortch et al., 2010).

The geology of the study area is closely related to the Denali Fault system, which developed in a former suture zone between the Paleozoic continent, and a Late Paleozoic island-arc system (Fig. 2; Richter and Jones, 1970; Csejtey, 1976). This fault system is one of North America's most prominent tectonic features, extending over 2000 km from SE Alaska to the Bering Sea (Stout and Chase, 1980) with a net fault slip of >38 km over the past 38 Myr (Stout et al., 1973; Reed and Lanphere, 1974). Cosmogenic exposure dating along the central sections of the Denali Fault indicates mean Late Quaternary slip rates of 12.0 ± 1.7 mm yr^{-1} (Matmon et al., 2006). The areas north of the Denali Fault are mainly composed of the Devonian-Mississippian and middle Paleozoic Yukon-Tanana terrane, comprising poly-metamorphosed, metasedimentary, and intermediate metavolcanic rocks, and lower Devonian and Mississippian metagranites (Fig. 2; Stanley et al., 1990). Bedrock south of the Denali Fault features Paleozoic and Mesozoic sedimentary and volcanic rocks (Hickman et al., 1978). The generally older rocks

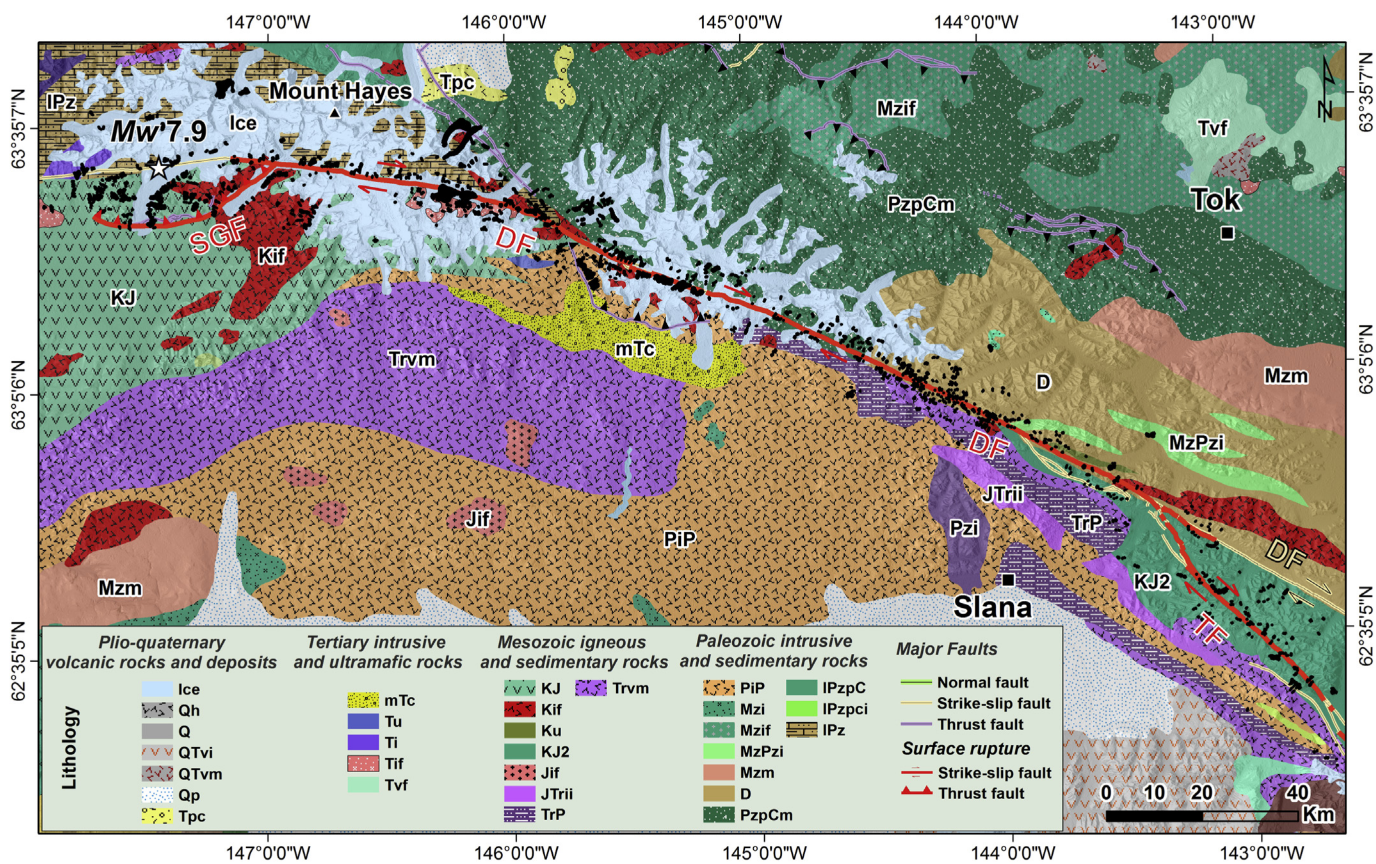

Fig. 2. Geologic map of the study area (after Beikman, 1980). Ice: Ice covered areas; Qh: Holocene deposits; Q: Quaternary deposits; Qp: Pleistocene alluvial and glacial deposits; QTvi: Quaternary or Tertiary trachytic to andesitic volcanic rocks; QTvm: Quaternary or Tertiary mafic volcanic (basaltic) rocks; mTc: Middle Tertiary continental sand-, silt-, claystones, and coal beds; Tu: Tertiary ultramafics; Ti: Tertiary undifferentiated intrusives; Tif: Tertiary granites to granodiorites; Tvf: Tertiary rhyolites and dacites; KJ: Cretaceous and Jurassic argillites, shales, and graywacke; Kif: Cretaceous granites to granodiorites; KJ2: Lower Cretaceous and upper Jurassic shallow and deep water clastic deposits; Ku: Cretaceous ultramafics; Jif: Jurassic felsic granites to granodiorites; JTrii: Jurassic and Triassic syenites to diorites; TrP: Triassic and Permian sand-, siltstones, and shales; Pip: Permian and Pennsylvanian basaltic to andesitic lavas and volcaniclastics; Mzi: Mesozoic undifferentiated intrusives; Mzif: Mesozoic granites to granodiorites; MzPzi: Mesozoic and paleozoic undifferentiated intrusives; Mzm: Mesozoic metamorphic rocks; D: Devonian undifferentiated volcanic rocks; lPzpC: Lower Paleozoic and Precambrian sand-, limestone, shale, chert, and phyllite; lPzpCi: Lower Paleozoic and Precambrian undifferentiated intrusives; lPz: Lower Paleozoic (incl. Cambrian to Devonian) rocks, with local greenschist and amphibolite facies.

along much of the north side of the Denali Fault indicate that the net vertical slip has been north side up (Stout et al., 1973). The high historic seismicity dominantly featured medium-sized shallow earthquakes; an average of four earthquakes of M > 3 occurred per year during the 30 years prior to the 2002 earthquake (Doser, 2004).

3. Methods

We mapped the locations and footprint areas of individual landslides from pre- and post-earthquake multi-spectral satellite images, and a Light Detection and Ranging (LiDAR)-derived digital terrain model (DTM) covering an area of ~22,000 km^2. To detect pre-earthquake landslides we used ASTER (with 15-m pixel resolution) and Landsat TM5 and ETM+ (both with 30-m pixel resolution) imagery taken between 1995 and 2003. Post-earthquake images included Earth Observing One (EO-1, with 30 m spatial resolution) data together with a 0.5-m LiDAR DTM covering the main affected region. The images had a fractional cloud and shadow cover of <1.2%. We used true-color composites and panchromatic images for monoscopic image interpretation, identifying individual slope failures by diagnostic features such as differences in shape, size, color, tone, texture, and landform assemblages (van Westen et al., 2008; Gorum et al., 2011). We also used oblique-aerial photos taken from aircraft shortly after the event (11/07/2002; USGS, 2002; http://ak.water.usgs.gov/glaciology/m7.9_quake/). We mapped 1580 coseismic landslides but suspect that many small landslides remained below the detection limit of the satellite images, especially in the western part of the study area.

In order to assess the role of topography and the surface-rupture process on the distribution of coseismic landslides, we obtained several terrain metrics and lithologic data (1:250,000 digital geological map by Wilson et al., 2008), and data on coseismic deformation. We computed landslide point density [km^{-2}], and the fraction of area affected by landslides within a 2-km radius using a Gaussian kernel density estimator. We derived local hillslope gradients from ASTER GDEM-2 data at 30-m pixel resolution using a best-fit plane in a 3 × 3 moving window, and estimated local topographic relief from the elevation range within a 2-km radius. These metrics are proxies of hillslope response and susceptibility to (coseismic) landsliding (Wolinsky and Pratson, 2005; Korup, 2008; Korup and Schlunegger, 2009), which we derived for areas with coseismic landslide density >0.01%. We also computed landscape ruggedness by measuring the dispersion of vectors normal to the terrain surface (Sappington et al., 2007).

We derived data on regional-scale coseismic deformation and fault-rupture process from a 3D-rupture model based on a joint inversion of geodetic and field based off-set measurements (Hreinsdottir et al., 2006). We also used inversion model results from the teleseismic body-wave data (Frankel, 2004) to determine the role of low and high seismic energy pulses on both size and abundance of the coseismic landslides.

4. Results

The 2002 Denali earthquake triggered at least 1580 landslides in an area of 7150 km^2, and up to ~380 km away from the epicenter. Directivity analysis reveals a distinct sub-parallel alignment of landslide scars with respect to the ruptured faults, with only few

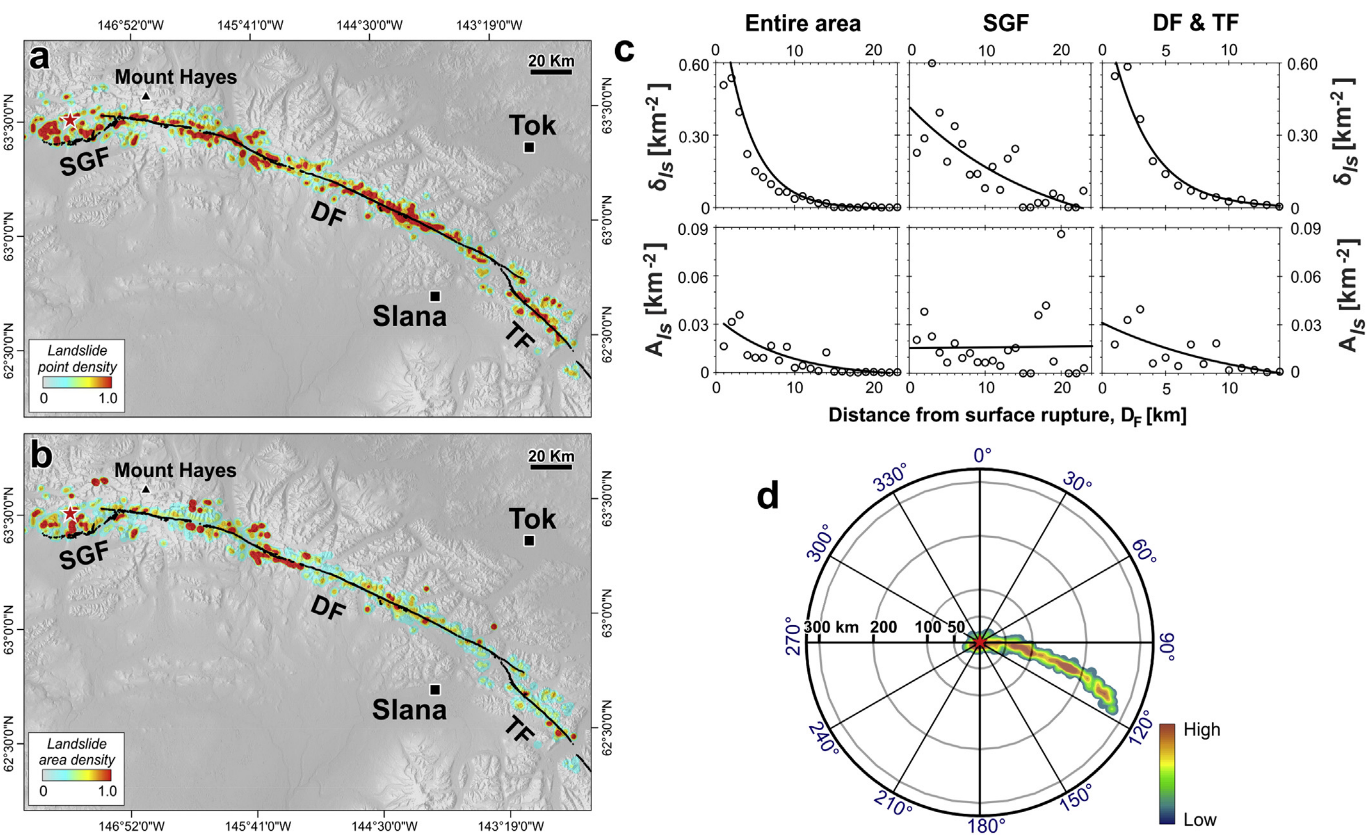

Fig. 3. Spatial pattern of 1580 landslides triggered by the 2002 Denali Fault M_w 7.9 earthquake, Alaska. (a) Normalized landslide point density δ_{ls} within 2-km radius. (b) Normalized landslide area density A_{ls} within 2-km radius. (c) Decay of δ_{ls} and A_{ls} with distance from surface ruptures; SGF: Susitna Glacier Fault, DF: Denali Fault, TF: Totschunda Fault. (d) Normalized directivity of landslides.

landslides occurring W of the epicenter: Most slope failures occurred along the dip-slip segment of the Susitna Glacier Fault (Fig. 3). The majority of these landslides clustered in a ~10-km wide corridor along the surface ruptures of the Susitna Glacier Fault, Denali Fault, and Totschunda Fault (Fig. 3a and b). About 80% of the total landslide-affected area is within ~7 km distance from the strike-slip segments (Denali Fault and Totschunda Fault), whereas this corridor is twice as wide in the thrust-dominated fault segments of the Susitna Glacier Fault (Fig. 3). Landslide density varies considerably along the rupture trace, but decays nonlinearly away from it (Fig. 3c). We discern three distinct zones of high coseismic slope instability: The first, near the epicenter on the Susitna Glacier Fault, contains 32% of all coseismic landslides that cover an area of ~22 km^2 in total. There, vertical displacement ranged from 0.2 to 5.4 m (Crone et al., 2004) in the first sub-event near the epicenter area on the Susitna Glacier Fault, and most landslides coincided with 1.5- to 5-m offsets (Fig. 4). Some 94% of the landslides occurred on the hanging wall up to 24 km away from the fault, mainly featuring rock slides and long-runout avalanches that detached from steep (>32°) slopes above West Fork Glacier, creating supraglacial deposit volumes of the order of 10^7 m^3 (Jibson et al., 2004, 2006; Fig. 5). The second landslide cluster includes nearly half (~42%) of the total affected slope-failure area, and is located near where the Trans-Alaska pipeline crosses the Denali Fault. There, five rock avalanches detached from near the McGinnis Peak and Black Rapids Glaciers (Fig. 6a and b), mobilizing several 10^7 m^3 of rock material (Jibson et al., 2006; Fig. 6b and c). Similarly large rock avalanches, with a total volume of 37 × 10^6 m^3, occurred S of the surface rupture on north-facing hillslopes of Black Rapids Glacier. A third, though not as pronounced, landslide cluster lies ~40 km W of the Denali Fault-Totschunda Faults junction, where the surface rupture is very linear (Fig. 7a). There, numerous shallow rock slides and falls occur S of the rupture trace, together with sackungen and mostly ridge-parallel tension cracks of different length (10–650 m) around Gillett Pass (Fig. 7a–c). Some of these scarps accommodate up to 7 m of displacement, and ridge-top trough and tensional anti-slope scarps formed along the surface rupture near the ridge crest (Fig. 7b and c). Altogether, however, the N block contains more landslides, with >65% concentrated on ESE-facing hillslopes (Fig. 7d and e).

We divided the surface-rupture trace into two sub-sections based on dominant fault-slip geometries, and normalized the data by rupture length of each fault type. We find that the western portion of the Susitna Glacier Fault, which is dominated by thrust faulting and high vertical coseismic offsets (with an average of ~3 m), has the higher normalized landslide density by area. Local decreases in landslide density are thus consistent with lower measured coseismic offsets (Fig. 4). Sub-events 1 and 2 are likely to have triggered >500 landslides within an area of ~80 km^2, which is about nine times more than that attributed to sub-event 3 (Fig. 4). Also, the largest high-frequency energy release per fault segment occurred in sub-events 1 and 2 (Frankel, 2004). Although the maximum horizontal displacements during the Denali earthquake were associated with the third sub-event, the landslide-affected area in this easternmost area is considerably lower (Fig. 4). However, when comparing the length of the rupture segment and the landslide abundance in these parts, sub-event 3 has higher landslide abundance.

Shallow rock falls and rock slides from steep slopes, involving the few upper meters of weathered bedrock or thin colluvium, dominate the spectrum of slope failures (Jibson et al., 2006). Cretaceous sandstone and limestone, Devonian pyroclastic rocks, and ice-covered areas host about half of all landslides in bedrock and Quaternary cover units. In terms of landslide densities, Tertiary granites and ice-covered areas were the most failure-prone units; this is also where some of the largest rock slides and rock avalanches occurred (Fig. 2; Table 1). Other common source areas included Devonian phyllites, graywackes, and sandstones that are

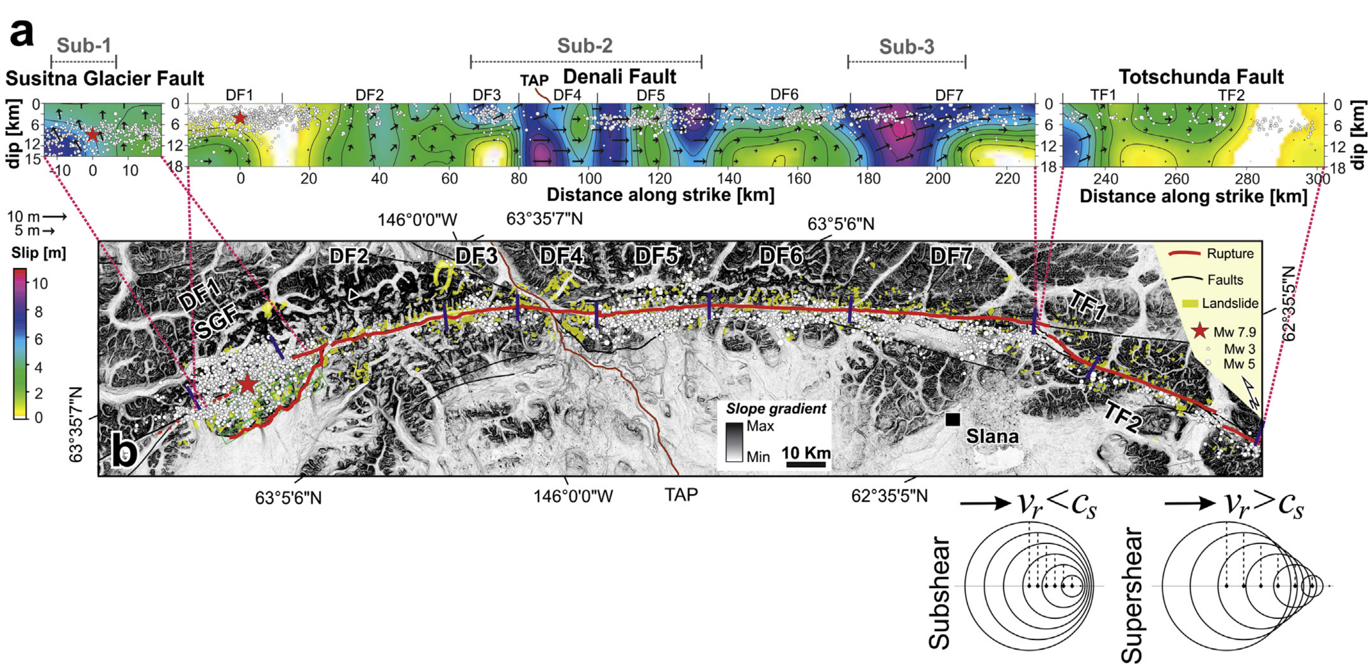

Fig. 4. Coseismic slip model and distribution of landslides triggered by the Denali Fault earthquake. (a) Coseismic slip model of the Denali Fault earthquake (Hreinsdottir et al., 2006), with slip distribution for Susitna Glacier Fault (SGF1-2); Denali Fault (DF1-7); and Totschunda Fault (TF1-2). Vectors give slip direction and scale of the N block relative to an observer on the S side (Hreinsdottir et al., 2006); star is epicenter; TAP: Trans-Alaska pipeline; faults after Plafker et al. (1994). (b) Distribution of coseismic landslides scaled to slip model, and location of sub-events. Relocated aftershocks (white dots) from Ratchkovski et al. (2003) are shown in both figures for reference. Inset illustrations (Dunham and Bhat, 2008) show shear wave fronts emitted where the rupture passes the solid dots. Rupture speed v_r is lower than S-wave speed, c_s, in case of sub-shear rupture, and vice versa for super-shear rupture.

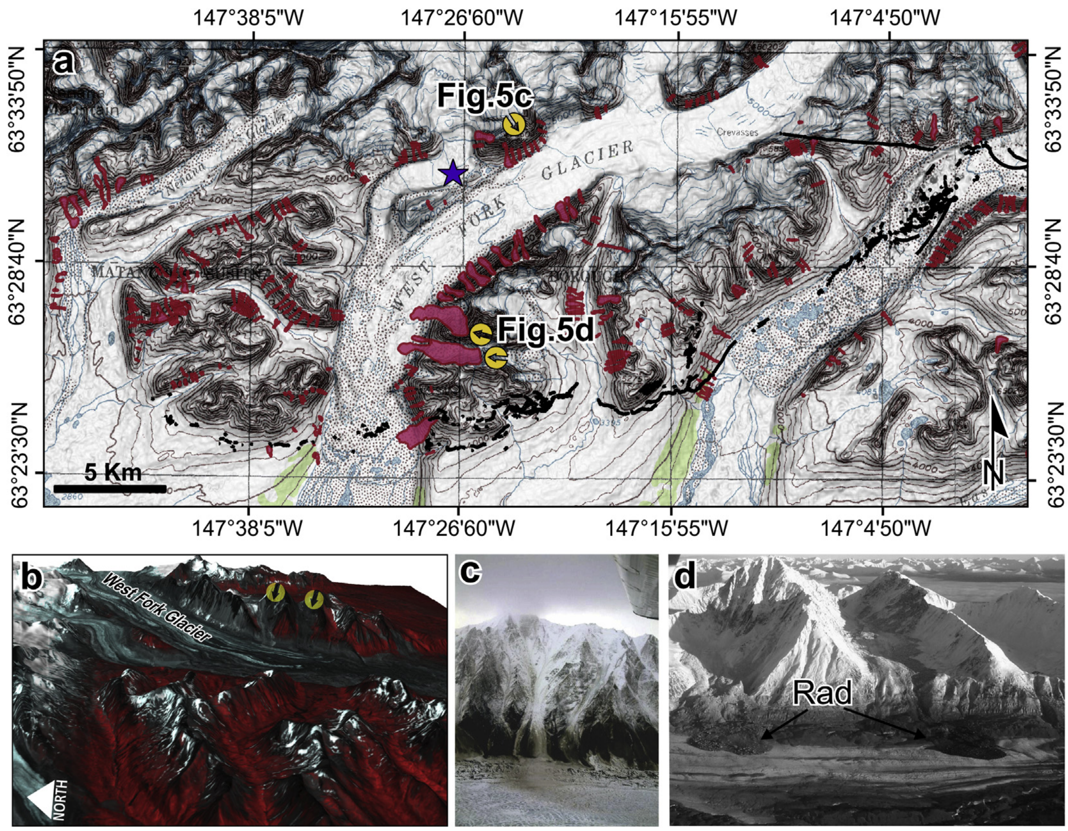

Fig. 5. (a) Coseismic landslides (red) in the Susitna Glacier Fault area. Star is location of Denali earthquake epicenter. (b) Post-seismic oblique false-color view of two large rock avalanches that occurred above West Fork Glacier. (c) Rock avalanches and rock falls on western slopes above West Fork Glacier (photo courtesy of USGS, 2002). (d) West Fork Glacier rock-avalanche deposits (RAD; photo courtesy of USGS, 2002). (For interpretation of the references to color in this figure legend, the reader is referred to the web version of this article.)

widely exposed in the W section of the surface rupture; there, some 65% of coseismic landslides occurred N of the surface rupture (Fig. 3a and b). Widespread Cretaceous sandstones, arkoses, and limestones gave rise to surprisingly few landslides, and Triassic to Tertiary sedimentary and ultramafic rocks were among the least affected in the study area. Less than a quarter of all landslides, though nearly half of the total landslide-affected area, occurred in glacierized terrain (see Supplementary Information Fig. S1 and Table S1). There, landslides descended from steeper and slightly higher slopes, and had longer runout.

In terms of topographic distribution, landslide abundance grows linearly with hillslope steepness S_h and local topographic relief H in the flatter and low-relief portions of the area, but increases in a scattered and nonlinear fashion above the modes of H and S_h (Fig. 8). Coseismic landslides occurred predominantly on hillslopes that were steeper than the modal slope gradient for the study area (Fig. 9a and b), irrespective of fault type. Overall, coseismic landslides initiated from steeper and more deeply dissected slopes at greater distance from the fault ruptures, although this trend largely coincides with major relief characteristics.

5. Discussion

5.1. Role of ice cover

The 2002 Denali earthquake raises questions about the role of glaciers in modulating seismic shaking and concomitant hillslope response through mass wasting. Numerical modeling results suggest that glacial ice may reduce topographic amplification of seismic shaking in mountainous terrain, where the ice thickness approaches the local slope height; deglaciation may create the opposite effect by exposing higher, oversteepened topographic relief (McColl et al., 2012). Such amplification is most pronounced for steeper slopes, and near ridges and mountaintops (Meunier et al., 2008; Gorum et al., 2013). Our finding that most landslides occurred in terrain of higher-than-average steepness and topographic relief supports earlier observations from other earthquake-impacted landscapes (Keefer, 2000; Korup, 2008; Buech et al., 2010; Iwahashi et al., 2012). However, those coseismic landslides that originated from ice-free rock slopes and narrow knife-edge ridges between glacial valleys had larger volumes and runout in the E section of the surface rupture (Supplementary Information Fig. S1, Table S1). This observation is consistent with observations from other supraglacial rock-slope failures that had higher runout that may have been aided by basal frictional melting of ice and snow that leading to higher pore water pressures in thin basal shear layers, even if not triggered by earthquakes (Clague and Evans, 1994; Schneider et al., 2011; Sosio et al., 2012).

Detailed, though currently unavailable, data on local ice thicknesses would help assess in more detail any potential buffering effects of the many cirque and valley glaciers on incoming seismic waves. In any case, the Denali earthquake produced nearly two orders of magnitude fewer landslides in a much narrower corridor along the fault ruptures than first-order empirical predictions for an M ~8 earthquake would suggest. Using the empirical relationship, based on all types of historic earthquakes, between the number of coseismic landslides and earthquake magnitude in Keefer (2002, Fig. 6), we obtain ~80,000 landslides for M_w 7.9, and

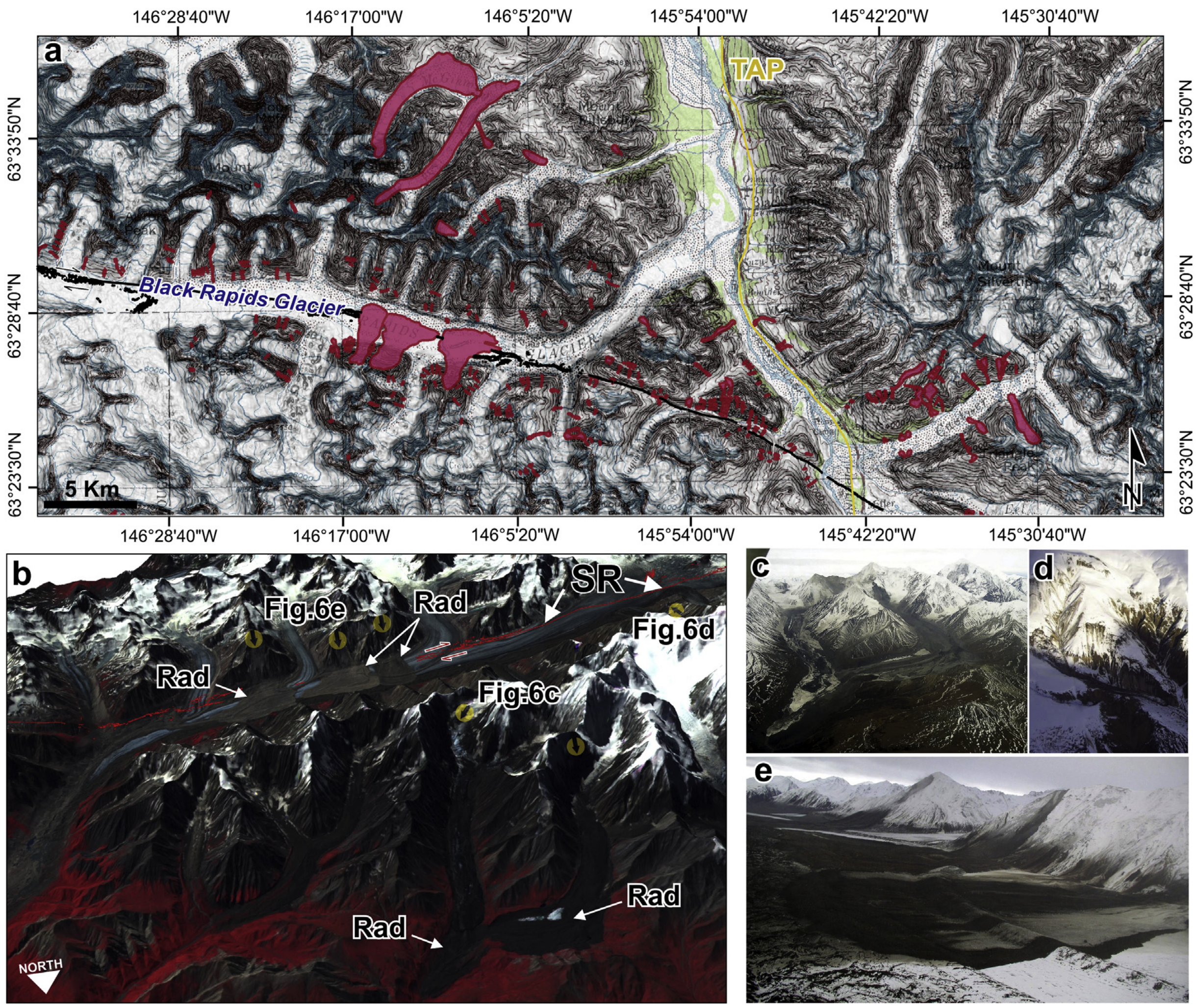

Fig. 6. (a) Coseismic landslides near Black Rapids Glacier; TAP: Trans-Alaska Pipeline. (b) Post-earthquake oblique false-color view of five large rock avalanche deposits (Rad) that straddle the Denali Fault; SR: Surface rupture. (c) Rock avalanches on flanks of McGinnis Peak (view toward SW) with runouts of up to ~6 km. (d) Small rock falls near Denali Fault. (e) Deposit of east Black Rapids rock avalanche (view toward SE). Photos (Fig. 5c-e) courtesy of USGS (2002).

~14,500 landslides for M_w 7.3. Thus, even if using the smallest sub-event magnitude for the Denali earthquake, the number of mapped landslides is an order of magnitude lower than the one predicted. Similar empirical relationships (Keefer, 2002) predict that a seismic energy release of this range in magnitudes would trigger landslides up to 250–350 km away from the fault, affecting an area of 30,000–95,000 km^2. Our mapping reveals that coseismic landslides occurred at a maximum distance of ~24 km from the fault, if excluding several minor failures near Nelchina River ~150 km from the fault, and that the total area affected by landslides was only 7150 km^2 despite widespread steep mountainous terrain prone to slope failure (Fig. 9). Similarly, the average estimated deposit thickness of the coseismic landslides was <1 m, while that of the larger rock avalanches rarely exceeded a few meters (Jibson et al., 2006). This would translate into a total landslide volume of >0.12 × 10^9 m^3, which is also considerably low given that earthquakes of comparable magnitudes have mobilized more than tenfold this volume (Fan et al., 2012). Therefore, we caution against jumping to conclusions when predicting landslide impact from earthquake magnitude alone.

While future work will be necessary to elucidate whether the subdued mass-wasting response to strong seismic shaking partly resulted from a glacial buffering effect, we cannot rule out moderating effects of the strike-slip, and near-vertically dipping, fault geometry that characterizes the Denali Fault earthquake. This geometry impedes distinct hanging-wall shattering effects that, for example, characterized the M_w 7.9 2008 Wenchuan earthquake, which triggered >60,000 landslides (Gorum et al., 2011). Both the Wenchuan and the Denali earthquakes had a similar magnitude and complex rupture process, although the Wenchuan earthquake occurred on faults dipping less steep, and in terrain largely devoid of glaciers (Fig. 12). Bearing these differences in fault geometry and ice cover in mind, the Wenchuan earthquake triggered, for a comparable magnitude, ~40 times as many landslides over an area nearly three times as large, and at distances of up to nearly five times farther away from the fault. To explore further potential controls of fault geometry on coseismic landslide generation, we compare our data with findings from other recent strike-slip earthquakes along near-vertically dipping faults in formerly glaciated and periglacial settings.

5.2. Comparison with recent strike-slip earthquakes

We compare our results with coseismic landslides inventories that we compiled following the 2010 M_w 6.9 Yushu, Tibet (Xu et al., 2013), and the 2007 M_w 6.2 Aysén Fjord, Chile, earthquakes using the

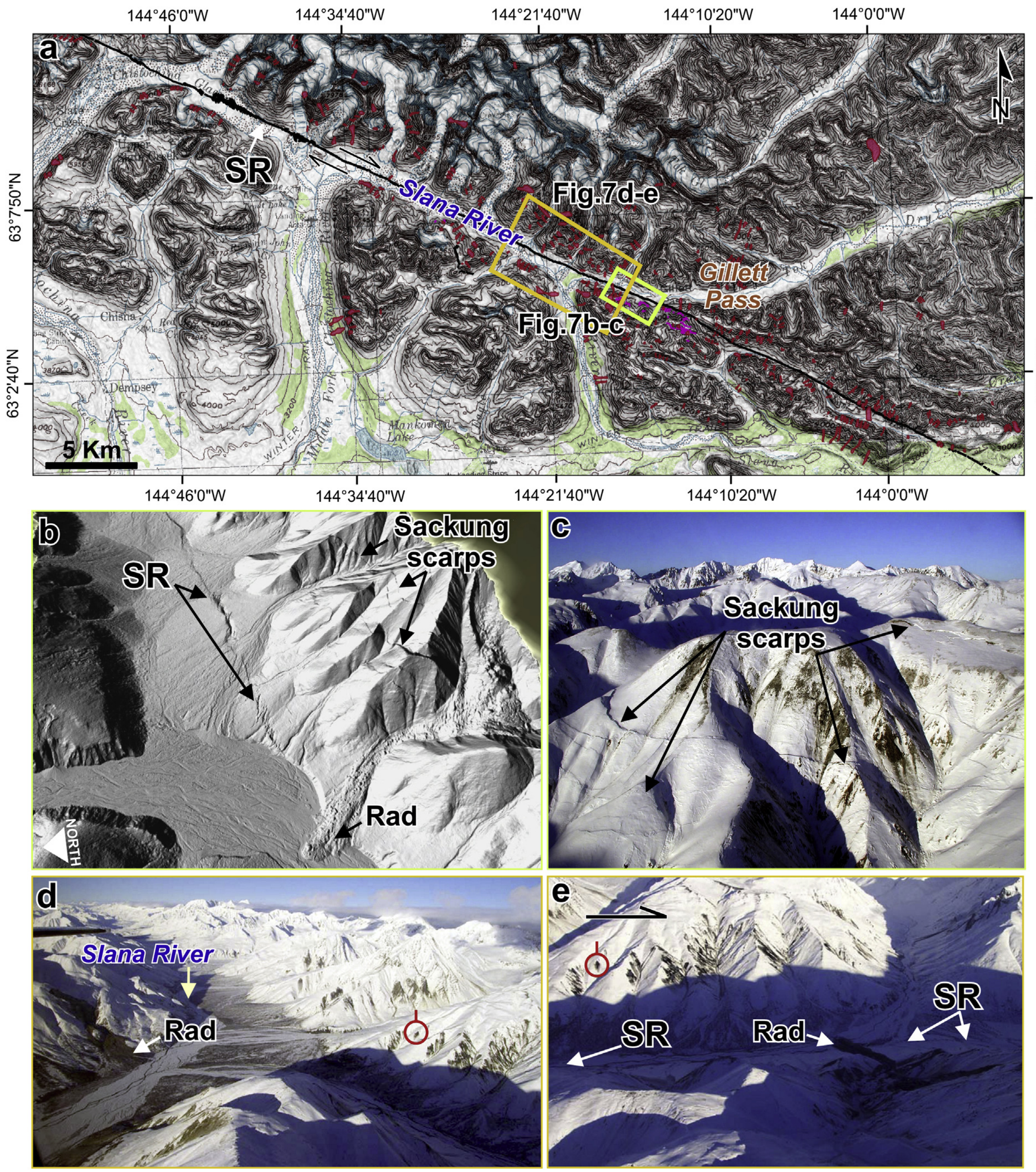

Fig. 7. (a) Coseismic landslides in Slana River valley and Gillett Pass area. (b) LiDAR DEM (courtesy of http://opentopography.org) shows rock-avalanche deposits (Rad) and multiple uphill-facing scarps on ridges along surface rupture of Denali Fault (SR). Rad: Rock avalanche deposit. (c) Oblique view of sackung scarps. (d) Rock falls near Denali Fault (view toward NW). (e) Different angle of rock falls near Denali Fault (view toward N); most coseismic landslides clustered N of the surface rupture on ESE facing hillslopes, i.e. consistent with the direction of rupture propagation (black arrow). Red circles show the same rock fall in both images. Photos (Fig. 6c–e) courtesy of USGS (2002). (For interpretation of the references to color in this figure legend, the reader is referred to the web version of this article.)

methods described above. Both events were dominated by strike-slip motion in periglacial and formerly glaciated (fjord) topography, respectively, and offer the opportunity of investigating of whether the spatial coseismic landslide pattern differs from that of the Denali earthquake in the absence of glaciers, given comparable types of fault motion, but lesser energy release. We find that the Yushu earthquake triggered a landslide pattern that similarly mimics variations in coseismic deformation as well as highest topographic relief and hillslope steepness (Fig. 10e–h). High landslide abundances in below-average local relief and hillslope steepness indicate that the control of slip was more prominent in the central section of the fault rupture (Fig. 10e and f). Despite these similarities to the Denali earthquake, the number of landslides attributed to the Yushu earthquake is slightly higher, i.e. ~2,040, mainly because of the ten-fold higher spatial resolution of the remote-sensing imagery used for mapping. Yet the total landslide-area affected area and the total volume of displaced material in the Yushu earthquake are two orders of magnitude less than those of

Table 1
Absolute and relative abundance of lithologic groups and coseismic landslides in the area affected by the 2002 Denali earthquake.

Lithology	Symbol	Landslide		Lithology				Landslide density %
		Frequency of landslides (N)	Frequency of landslides (%)	Total area A (km^2)	%	Total area A (km^2)	%	
Ice covered areas	Ice	300	18.99	58.51	48.23	2332.59	33.23	1.76
Ultramafic rocks (Tertiary)	Tu	2	0.13	0.05	0.04	16.98	0.24	0.19
Undifferentiated intrusive rocks (Tertiary)	Ti	5	0.32	0.92	0.76	41.53	0.59	1.55
Granite to granodiorite (Tertiary)	Tif	58	3.67	7.07	5.83	91.67	1.31	5.41
Argillite, shale, greywacke, quartzite, conglomerate (Cretaceous)	KJ	209	13.23	11.45	9.44	498.56	7.10	1.61
Granite to granodiorite (Cretaceous)	Kif	148	9.37	7.44	6.13	441.88	6.30	1.18
Ultramafic rocks (Cretaceous)	Ku	6	0.38	0.29	0.24	23.15	0.33	0.87
Sandstone, arkose, siltstone, and limestone (Lower Cretaceous)	KJ2	212	13.42	6.96	5.74	1018.77	14.52	0.48
Argillite, limestone, siltstone, conglomerate, and abundant gabbroic sills (Triassic)	TrP	25	1.58	0.69	0.57	304.92	4.34	0.16
Basalt (Triassic)	Trvm	53	3.35	1.23	1.01	320.59	4.57	0.27
Basaltic to andesitic lavas (Permian)	PIP	65	4.11	5.88	4.85	371.06	5.29	1.11
Undifferentiated intrusive rocks (Mesozoic and Paleozoic)	MzPzi	12	0.76	1.19	0.98	75.45	1.07	1.11
Pyroclastic rocks and ash flows interbedded with sedimentary rocks (Devonian)	D	268	16.96	6.63	5.46	749.59	10.68	0.62
Schist and gneiss (Paleozoic and (or) Precambrian)	PzpCm	129	8.16	8.66	7.14	447.84	6.38	1.36
Limestone, dolomite, argillite, chert, and graywacke (Lower Paleozoic)	IPz	88	5.57	4.35	3.58	283.99	4.05	1.07

the Denali earthquake (Fig. 11a–k; see Supplementary Information Table S2). This result reflects not only the shorter surface rupture and less coseismic slip of the Yushu earthquake, but also the less steep and long slopes that characterize the semiarid headwaters of the Jinsha/Yangtze River on the Tibetan Plateau, where alpine permafrost occurs above ~4300 m a.s.l. (Jin et al., 2007). Clearly, steeper and longer hillslopes are more prone to collapse during strong seismic ground shaking. Comparison of landslide inventories of strike-slip faulting earthquakes shows that coseismic slip, differences and variations in fault geometry (dip, strike, and slip mode), and local relief may control the size- and spatial distribution of coseismic landslides; both the Denali and Yushu earthquakes produced landsliding limited to a thin corridor flanking the rupture zones (Fig. 11a–g). Unlike dip-slip earthquakes, the strain in strike-slip earthquakes localizes to narrow segments which are wider near the surface than at depth, representing flower structures.

We obtained very similar results for the 2007 M_w 6.2 Aysén Fjord, Chile, earthquake, although the control of fault geometry on landslide distribution was more complex (Fig. 11h–j). The more scattered landslide distribution in Aysén Fjord as compared to the Denali and Yushu earthquakes can be explained by a rupture process involving slip on multiple gently dipping faults (Agurto et al., 2012). Although the Aysén Fjord earthquake was shallow, it did not rupture the surface, causing a less distinct coseismic landslide pattern. Despite the few available data on the rupture processes of this earthquake, the occurrence of fewer but larger landslides likely results from the high local relief and the steepness of slopes. We also stress that more landslides occurred in segments where strike-slip type of faulting formed step-over and bend structures, which supports the notion that local geometric variations of the surface rupture control the first-order pattern of coseismic landsliding (Figs. 4 and 11).

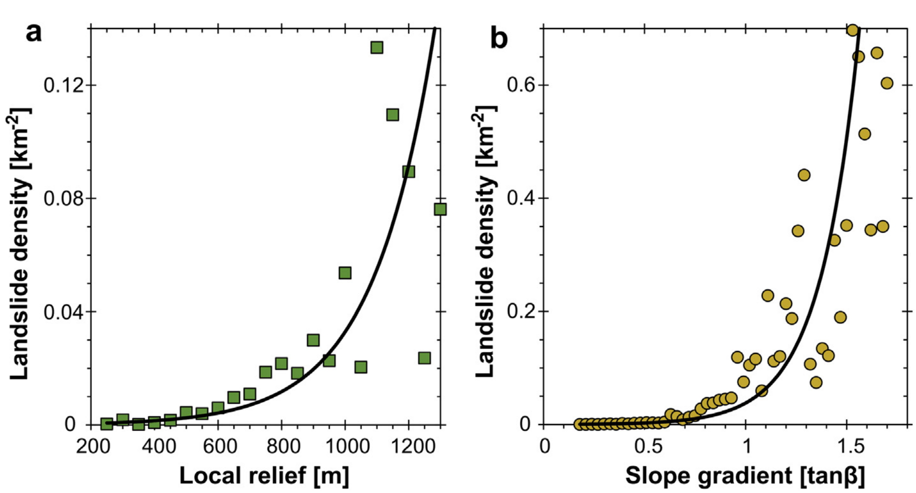

Fig. 8. Landslide area density versus local relief (a) and slope gradient (b). Exponential fit for visual guidance only.

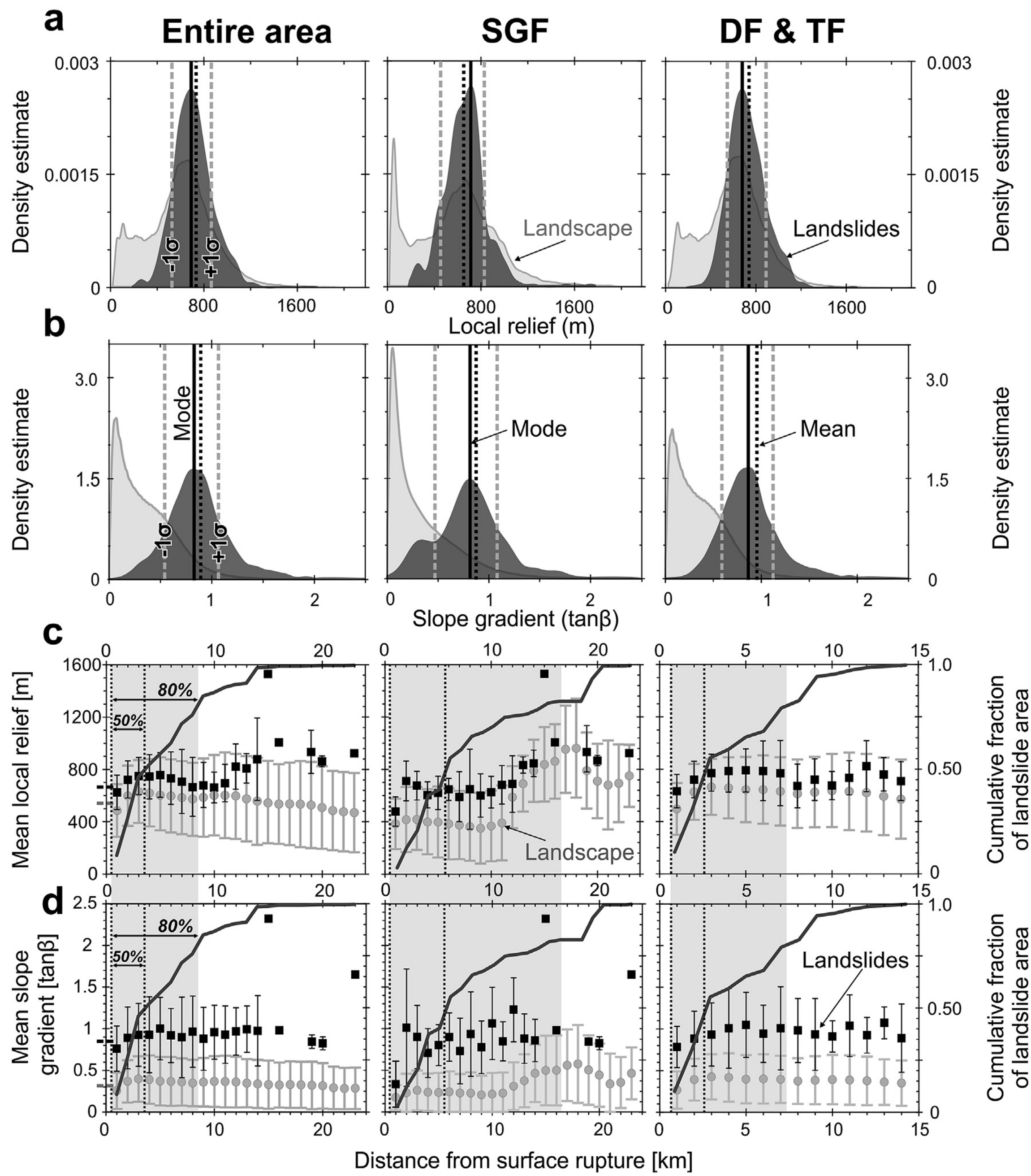

Fig. 9. Probability density estimates of local relief (a), and hillslope gradient (b) in the entire study area, and subsets defined by fault systems identified in Fig. 1. Light and dark gray shades are distributions of metrics for study area and landslides, respectively. Mean local relief (c) and hillslope gradient (d) of landslides and landscape in equal-width distance bins from surface rupture; secondary *y*-axis shows cumulative fraction of landslide area. Light gray boxes and dashed black lines delimit 80% and 50% of cumulative fraction of landslide area, respectively.

5.3. Coseismic landslide pattern and fault-rupture processes

Our data point to fault geometry and rupture process as key controls on the spatial pattern of coseismic landsliding. The confinement of coseismic landslides to a narrow corridor that, depending on fault mechanism, is only 7–15 km wide despite sufficiently steep terrain reflects roughly exponential seismic wave attenuation. Directivity analysis underlines that the string-like pattern of regional landsliding is consistent with the direction of fault-rupture propagation (Figs. 3 and 9). Abundant failures on hillslopes with ESE-facing aspect further agree with the dominant direction of coseismic slip, which may have caused greater ground-motion amplitudes on those slopes (Fig. 7d and e). Along traces of the fault ruptures, however, coseismic landslide abundance and density show a decisively peaked pattern. This finding is consistent with other studies that also show distinct clustering of 70–85% of slope failures triggered by intermediate- and large-sized earthquakes over the surface projection (up- and down-dip edge) of the faults, e.g. during the 1989 Loma Prieta, United States (M_w 6.9; Keefer, 2000), 1999 Chi-Chi, Taiwan (M_w 7.6; Hung, 2000); and 2008 Wenchuan, China (M_w 7.9; Gorum et al., 2011) earthquakes. These landslides pattern are thought to reflect the segments of

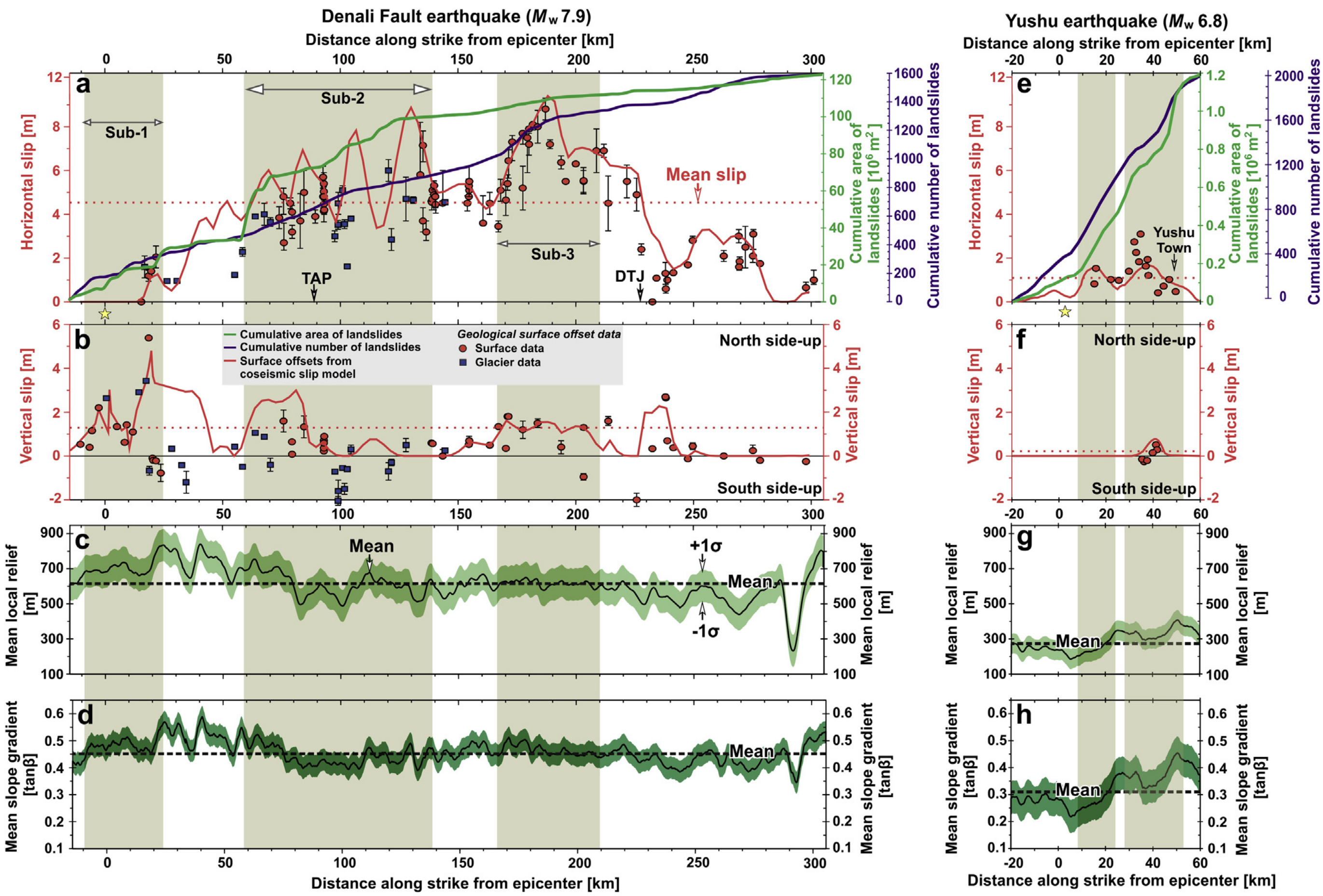

Fig. 10. Distribution of coseismic landslides, modeled coseismic slip, and topography along the Denali Fault and Yushu strike-slip earthquakes. (a) Modeled horizontal (right-lateral) slip amplitudes (Hreinsdottir et al., 2006) of Denali Fault earthquake and cumulative number (purple lines) and area (green lines) of coseismic landslides in 3-km bins; fault offset data (red circles and blue squares) from Haeussler et al. (2004). (b) Modeled vertical (reverse) slip amplitudes of Denali Fault earthquake (Crone et al., 2004; Hreinsdottir et al., 2006). (c) and (d) Swath profiles (40 km × 340 km) of mean local relief and mean slope gradient computed from ASTER GDEM-2 elevation data within 3-km radius. Black lines and green shading are means and ±1 standard deviations per 60-m bins; gray boxes delimit sub-events of Denali Fault earthquake. TAP: Trans-Alaska Pipeline. DTJ: Denali-Totschunda fault junction. (e) Modeled horizontal (left-lateral) slip amplitudes (Li et al., 2011); all other signatures as in (a). Geological offset data (red circles) after Lin et al. (2011). (f) Modeled vertical (reverse) slip amplitudes (Li et al., 2011). (g) and (h) Swath profiles (20 km × 80 km) derived as described in (c) and (d); dark gray boxes delimit high slip patches of Yushu earthquake. (For interpretation of the references to color in this figure legend, the reader is referred to the web version of this article.)

differing fault geometry, especially in complex earthquake rupture sequences, involving more than one fault type (Gorum et al., 2013; Fig. 12). Yet the abundance and density of the coseismic landslides also strongly vary along the surface ruptures, and possibly reflecting non-uniform frictional strength along the fault plane. Thus overall displacement involves slip on one or more asperities, i.e. high-slip patches, where friction is at its maximum (Hall-Wallace, 1998). Most of the energy released during earthquakes is tied to these asperities (Ruiz et al., 2011). Our results show a spatial coincidence of landslide abundance with the rate and mode of coseismic deformation, and also with hillslope steepness and topographic relief. Step changes in cumulative area and in the number of the coseismic landslides coincide with such asperities, and contain ~85% of the landslide-affected areas (Figs. 4 and 10).

Although the highest displacements were measured in sub-event 3, landslide density is lowest compared to that of the preceding two sub-events (Fig. 10a, Sub-3). This discrepancy is likely due to differing modes and rates of coseismic slip, rupture velocities, and topography during these sub-events. Vertical slip in the first two sub-events was higher than in sub-event 3 (Fig. 10b). Coseismic slip directions are fault-normal and therefore have compressive strain in sub-event 1. In contrast, sub-event 2 has a transition character: Particularly where landslides abound, coseismic slip directions are fault-parallel with high shear strain and above-average vertical displacement (Figs. 4a and 10b). In sub-event 3, horizontal displacements dominate the linear surface rupture. In addition, while velocity values were <3.5 km s^{-1} in sub-events 1 and 2, sub-event 3 was characterized by super-shear with effective rupture velocities of ~5.0 km s^{-1}, and thus larger than S-wave speeds (Frankel, 2004). Rupture speed determines how waves from different parts of the fault interfere with each other. During sub-shear wave fronts are concentrated in the forward direction and separated in the backward direction (Fig. 4), leading to larger amplitudes and higher frequencies in the forward direction (Dunham and Archuleta, 2004; Dunham and Bhat, 2008). For super-shear ruptures, the source outruns the waves, and a Mach front is formed (Dunham and Bhat, 2008). These changes in rupture velocities are consistent with spatial changes in landslide density, which is high during the first two sub-events. Super-shear velocities during sub-event 3 were associated with a decrease in the generation of high-frequency energy (Frankel, 2004), and are consistent with theoretical work (Burridge et al., 1979). In addition,

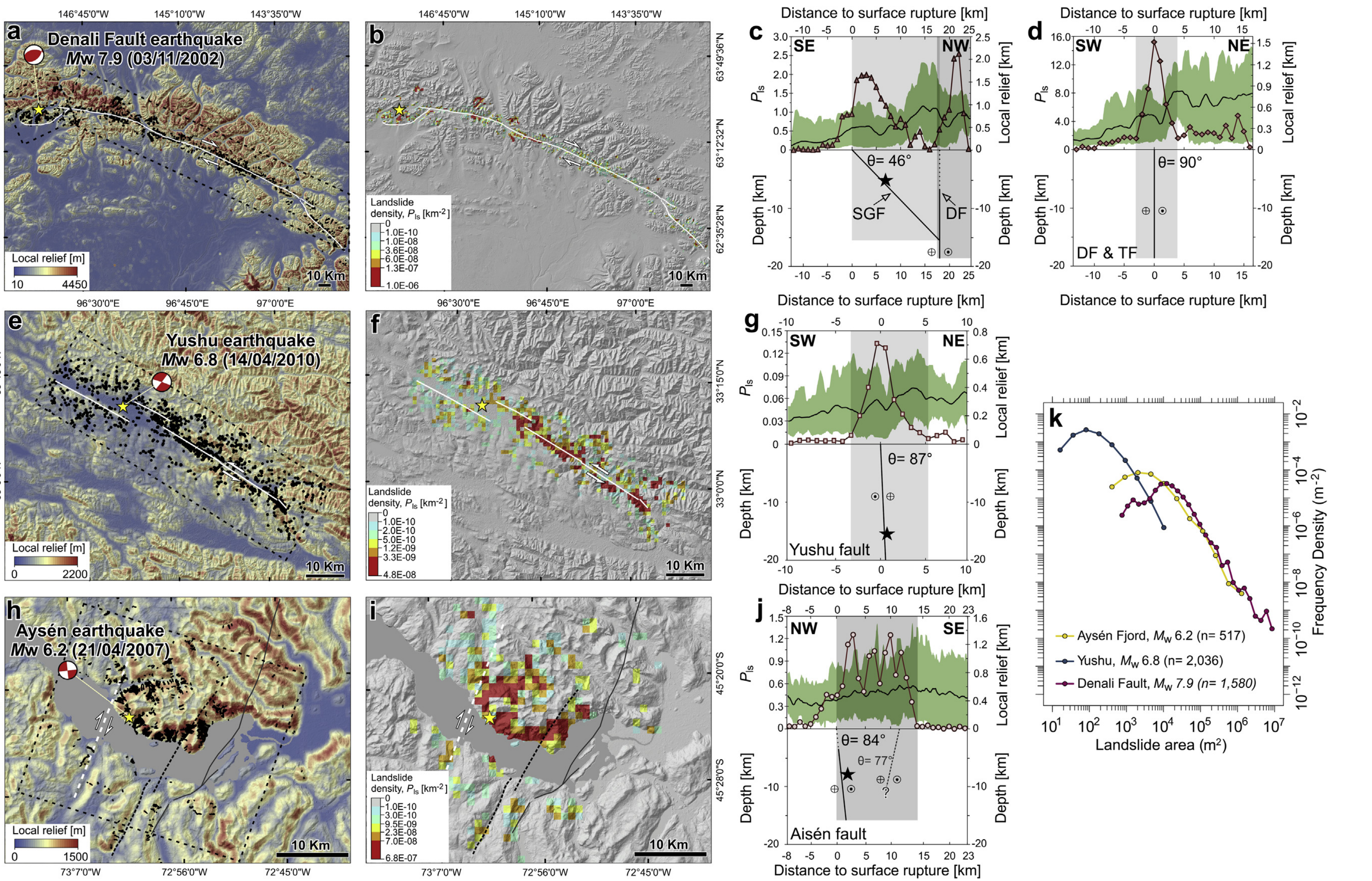

Fig. 11. Comparison of fault geometry with landslide point density (P_{ls}), and local relief along transverse swath profiles for (a)–(d) Denali Fault, (e)–(g) Yushu and (h)–(j) Aysén Fjord strike-slip earthquakes. Dashed rectangles are locations of transverse swath profiles (c, d, g, and j). Thick black line and green shading are mean, minimum, and maximum local relief, respectively, computed for 60-m bins. Landslide density P_{ls} (dark red lines) defined as $P_{ls} = A_{ls} / A_t$ where A_{ls} is the area of all landslides within a chosen window size A_t (Meunier et al., 2008). Stars are locations earthquake hypocenters. (k) Size distributions of log-binned landslide deposit areas for the three strike-slip earthquakes. (For interpretation of the references to color in this figure legend, the reader is referred to the web version of this article.)

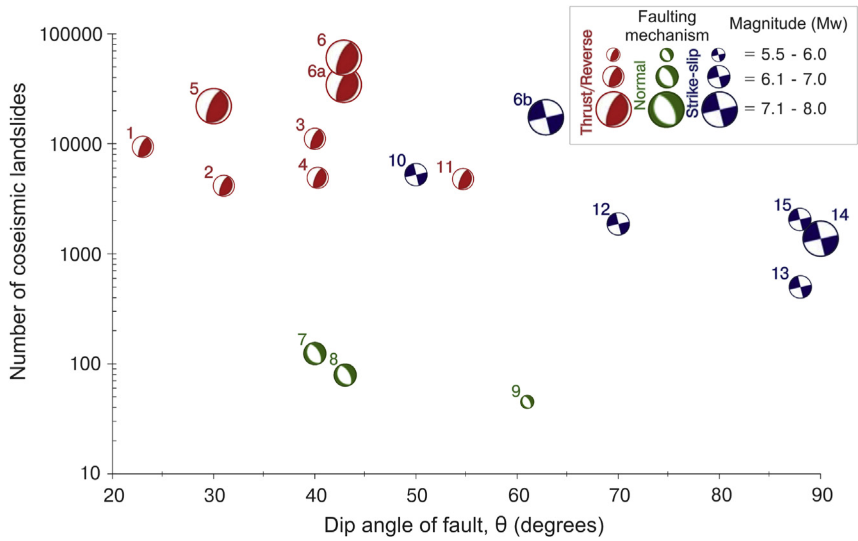

Fig. 12. Total number of earthquake-triggered landslides as a function of earthquake magnitude, dip angle, and faulting mechanism. 1: M_w 6.5 Coalinga, USA (1983); 2: M_w 6.9 Iwate-Miyagi Nairiku, Japan (2008); 3: M_w 6.7 Northridge, USA (1994); 4: M_w 7.0 Haiti (2010); 5: M_w 7.6 Chi-Chi, Taiwan (1999); 6: M_w 7.9 Wenchuan, China (2008); 6a: Reverse-slip segment, and 6b: Strike-slip segment; 7: M_w 6.0 Umbria Marche, Italy (1997); 8: M_w 6.3 L'Aquila, Italy (2009); 9: M_w 5.6 Rotoehu, New Zealand (2004); 10: M_w 6.2 Mammoth Lakes, USA (1980); 11: M_w 6.7 Mid-Niigata Prefecture, Japan (2004); 12: M_w 6.9 Loma Prieta, USA (1989); 13: M_w 6.2 Aysén, Chile (2007); 14: M_w 7.9 Denali, Alaska, USA (2002); 15: M_w 6.8 Yushu, China (2010).

lower local relief and hillslope steepness further are consistent with lower landslide abundance in the E part of the surface rupture (Fig. 10c and d).

We infer that our coseismic landslide inventory provides a unique opportunity to characterize the propagation direction of the surface rupture. The distribution pattern of the 1580 landslides shows a distinct sub-parallel clustering with respect to the ruptured faults. The strikingly few landslides occurring W of the epicenter area indicates that the dominant direction of the seismic waves could have caused ESE increases of the ground-motion amplitudes.

6. Conclusions

Our data highlight the spatial collocation of abundance, distribution pattern and the size of coseismic landslides with fault geometry and coseismic slip amplitudes in earthquakes with strike-slip motion. Analysis of the 2002 Denali Fault (M_w 7.9) earthquake shows that differences in fault geometry (dip, strike, and slip mode), together with local topography contribute to laying out the spatial pattern of coseismic landslides that straddle the surface ruptures dominated by strike-slip motion along narrow corridors. The Denali earthquake triggered ~1580 landslides, of which 80% happened <15 km from the surface rupture over its 300-km length; some 20% occurred in glacierized terrain. However, the total landslide number is an order of magnitude below that predicted for earthquakes of such magnitude (e.g. Keefer, 2002). The 2008 Wenchuan earthquake triggered nearly 40 times as many landslides over an area three times larger for a comparable magnitude, although the ruptured faults dipped less steep, and ice cover was largely absent. Distinct clusters of slope failures coincided spatially with high coseismic slip, local relief, and slope steepness. This spatial pattern largely reflects properties of the fault geometry. We argue that differences in rupture velocities between the three rupture sub-events may elevate the fraction of area affected by slope failures.

Comparing the Denali Fault earthquake with other strike-slip faulting events strengthens the view that the distribution pattern, abundance, and area affected by coseismic landslides reflect the fault geometry and type (Table S2; Fig. 12), rate and mode of displacements along the surface ruptures. Superimposed effects of local valley relief, hillslope steepness, and variations in rock type confirm this observation. Yet the role of glacial buffering of incoming seismic waves (McColl et al., 2012) warrants future research. We conclude that the variance contained in the resulting frequency-size distributions of coseismic landslides (Fig. 11k) may be a guide for future work on considering the seismic properties (i.e. magnitude, faulting mechanism, and rupture dynamics) and topographic characteristics together, rather than solely focusing on earthquake magnitude as a predictor of slope instability. Overall, our observations on coseismic landslide clustering and size-frequency distributions for strike-slip earthquakes call for refined empirical relationships between landslide frequency and earthquake magnitude (e.g. Rodrìguez et al., 1999; Keefer, 2002). Any prediction of earthquake-triggered sediment input into the glacial system solely based on earthquake magnitude is bound to result in potential order-of-magnitude misestimates, and thus remains problematic. Clearly, more research is needed to decipher the process feedbacks between fault geometry and rupture characteristics, glacier extent, and the fate of earthquake-generated sediment in this regard.

Acknowledgments

This work was supported by the United Nations University – ITC Center for Spatial Analysis for Disaster Risk Management (www.itc.nl/unu-drm). O.K. acknowledges support by the Potsdam Research Cluster for Georisk Analysis, Environmental Change and Sustainability (PROGRESS). We thank Tim Davies, John Clague, and Alexander Strom for their instructive and thought-provoking comments on an earlier version of this manuscript.

Appendix A. Supplementary data

Supplementary data related to this article can be found at http://dx.doi.org/10.1016/j.quascirev.2014.04.032.

References

Agurto, H., Rietbrock, A., Barrientos, S., Bataille, K., Legrand, D., 2012. Seismo-tectonic structure of the Aysén Region, Southern Chile, inferred from the $M_W = 6.2$ Aysén earthquake sequence. Geophys. J. Int. 190, 116–130.
Beikman, H.M., 1980. Geological Map of Alaska. U.S. Geological Survey, 1 Sheet, Scale 1:2,500,000. http://www.dggs.alaska.gov/pubs/id/20521.
Buech, F., Davies, T.R., Pettinga, J.R., 2010. The Little Red Hill seismic experimental study: topographic effects on ground motion at a bedrock-dominated mountain Edifice. Bull. Seismol. Soc. Am. 100, 2219–2229.
Burridge, R., Conn, G., Freund, L.B., 1979. The stability of a plane strain shear crack with finite cohesive force running at intersonic speeds. J. Geophys. Res. 84, 2210–2222.
Capps, S.R., 1940. Geology of the Alaska railroad region. United States Department of the Interior. Geol. Surv. Bull. 907, 1–201.
Clague, J.J., Evans, S.G., 1994. Formation and failure of natural dams in the Canadian Cordillera. Geol. Surv. Can. Bull. 464, 35.
Crone, A.J., Personius, S.F., Craw, P.A., Haeussler, P.J., Staft, L.A., 2004. The Susitna glacier thrust fault: characteristics of surface ruptures on the fault that initiated the 2002 Denali Fault earthquake. Bull. Seismol. Soc. Am. 94, 5–22.
Csejtey, B., 1976. Tectonic implications of a Late Paleozoic volcanic arc in the Talkeetna Mountains, south-central Alaska. Geology 4, 49–52.
Dortch, J.M., Owen, L.A., Caffe, M.W., Brease, P., 2010. Late Quaternary glaciation and equilibrium line altitude variations of the McKinley River region, central Alaska Range. Boreas 39, 233–246.
Doser, D.I., 2004. Seismicity of the Denali-Totschunda fault zone in Central Alaska (1912–1988) and its relation to the 2002 Denali Fault earthquake sequence. Bull. Seismol. Soc. Am. 94, S132–S144.
Dunham, E.M., Archuleta, R.J., 2004. Evidence for a supershear transient during the 2002 Denali Fault earthquake. Bull. Seismol. Soc. Am. 94, 256–268.
Dunham, E.M., Bhat, H.S., 2008. Attenuation of radiated ground motion and stresses from three-dimensional supershear ruptures. J. Geophys. Res. 113, B08319 http://dx.doi.org/10.1029/2007JB005182.
Eberhart-Phillips, D., Sieh, K., Rubin, C., 2003. The 2002 Denali Fault earthquake, Alaska. Science 300, 1113–1118.
Evans, S.G., Tutubalina, O.V., Drobyshev, V.N., et al., 2009. Catastrophic detachment and high-velocity long-runout flow of Kolka Glacier, Caucasus Mountains, Russia in 2002. Geomorphology 105, 314–321.
Fan, X., van Westen, C.J., Korup, O., et al., 2012. Transient water and sediment storage of the decaying landslide dams induced by the 2008 Wenchuan earthquake, China. Geomorphology 171–172, 58–68.
Fischer, L., Huggel, C., Kääb, A., Haeberli, W., 2013. Slope failures and erosion rates on a glacierized high-mountain face under climatic changes. Earth Surf. Processes Landf. 38, 836–846.
Frankel, A., 2004. Rupture process of the M7.9 Denali Fault, Alaska, earthquake: subevents, directivity, and scaling of high-frequency ground motions. Bull. Seismol. Soc. Am. 94, 234–255.
Gorum, T., Fan, X., van Westen, C.J., Huang, R., Xu, Q., Tang, C., Wang, G., 2011. Distribution pattern of earthquake-induced landslides triggered by the 12 may 2008 Wenchuan earthquake. Geomorphology 133, 152–167.
Gorum, T., van Westen, C.J., Korup, O., van der Meijde, M., Fan, X., van der Meer, F.D., 2013. Complex rupture mechanism and topography control symmetry of mass-wasting pattern, 2010 Haiti earthquake. Geomorphology 184, 127–138.
Haeussler, P., Schwartz, D., Dawson, T., et al., 2004. Surface rupture and slip distribution of the Denali and Totschunda Faults in the 3 November 2002 M 7.9 Earthquake, Alaska. Bull. Seismol. Soc. Am. 94, 23–52.
Hall-Wallace, M.K., 1998. Can earthquake be predicted? J. Geosci. Educ. 46, 439–449.
Harp, E.L., Jibson, R.W., Kayen, R.E., et al., 2003. Landslides and liquefaction triggered by the M 7.9 Denali Fault earthquake of 3 November 2002. GSA Today 13, 4–10.
Hewitt, K., 1999. Quaternary moraines vs catastrophic rock avalanches in the Karakoram Himalaya, northern Pakistan. Quat. Res. 51, 220–235.
Hewitt, K., 2009. Rock avalanches that travel onto glaciers and related developments, Karakoram Himalaya, Inner Asia. Geomorphology 103, 66–79.
Hickman, R.G., Craddock, C., Sherwood, K.W., 1978. The Denali Fault system and the tectonic development of southern Alaska. Tectonophysics 47, 247–273.
Hreinsdottir, S., Freymueller, J.T., Burgmann, R., Mitchell, J., 2006. Coseismic deformation of the 2002 Denali Fault earthquake: insights from GPS measurements. J. Geophys. Res. 111 (B03308), 1–18.
Hung, J.J., 2000. Chi-chi earthquake induced landslides in Taiwan. Earthq. Eng. Eng. Seismol. 2, 25–33.
Iwahashi, J., Kamiya, I., Yamagishi, H., 2012. High-resolution DEMs in the study of rainfall-and earthquake-induced landslides: use of a variable window size method in digital terrain analysis. Geomorphology 153, 29–38.
Jibson, R.W., Harp, E.L., Schulz, W., Keefer, D.K., 2004. Landslides triggered by the 2002 M-7.9 Denali fault, Alaska, earthquake and the inferred nature of the strong shaking. Earthq. Spectra 20, 669–691.
Jibson, R.W., Harp, E.L., Schulz, W., Keefer, D.K., 2006. Large rock avalanches triggered by the M 7.9 Denali Fault, Alaska, earthquake of 3 November 2002. Eng. Geol. 83, 144–160.
Jin, H.J., Chang, X.L., Wang, S.L., 2007. Evolution of permafrost on the Qinghai-Xizang (Tibet) Plateau since the end of the Pleistocene. J. Geophys. Res. 112, F02S09 http://dx.doi.org/10.1029/2006JF000521.
Keefer, D.K., 2000. Statistical analysis of an earthquake-induced landslide distribution the 1989 Loma Prieta, California event. Eng. Geol. 58, 231–249.
Keefer, D.K., 2002. Investigating landslides caused by earthquakes – a historical review. Surv. Geophys. 23, 473–510.
Korup, O., 2008. Rock type leaves topographic signature in landslide-dominated mountain ranges. Geophys. Res. Lett. 35, L11402 http://dx.doi.org/10.1029/2008GL034157.
Korup, O., Schlunegger, F., 2009. Rock-type control on erosion-induced uplift, eastern Swiss Alps. Earth Planet. Sci. Lett. 278, 278–285.
Li, Z., Elliott, J.R., Feng, W., Jackson, J.A., Parsons, B.E., Walters, R.J., 2011. The 2010 M_W 6.8 Yushu (Qinghai, China) earthquake: constraints provided by InSAR and body wave seismology. J. Geophys. Res. B116, 1978–2012.
Lin, A., Rao, G., Jia, D., Yan, B., Ren, Z., 2011. Co-seismic strike-slip surface rupture and displacement produced by the 2010 M_W 6.9 Yushu earthquake, China, and implications for Tibetan tectonics. J. Geodyn. 52, 249–259.
Matmon, A., Schwartz, D.P., Haeussler, P.J., et al., 2006. Denali fault slip rates and Holocene-Late Pleistocene kinematics of central Alaska. Geology 34, 645–648.
McColl, S.T., Davies, T.R.H., McSaveney, M.J., 2012. The effect of glaciation on the intensity of seismic ground motion. Earth Surf. Processes Landf. 37, 1290–1301.
Menounos, B., Clague, J.J., Clarke, G.K.C., et al., 2013. Did rock avalanche deposits modulate the Late Holocene advance of Tiedemann Glacier, southern Coast Mountains, British Columbia, Canada? Earth Planet. Sci. Lett. 384, 154–164.
Meunier, P., Hovius, N., Haines, A.J., 2008. Topographic site effects and the location of earthquake-induced landslides. Earth Planet. Sci. Lett. 275, 221–232.
Ozacar, A.A., Beck, S.L., 2004. The 2002 Denali Fault and 2001 Kunlun Fault earthquakes: complex rupture processes of two large strike-slip events. Bull. Seismol. Soc. Am. 94, 278–292.
Plafker, G., Moore, J.C., Winkler, G.R., 1994. Geology of the southern Alaska margin. In: Plafker, G., Berg, H.C. (Eds.), Geology of North America, vol. G-1. Boulder, Colorado, Geological Society of America, The Geology of Alaska, pp. 389–449.
Ratchkovski, N.A., Hansen, R.A., Stachnik, J.C., et al., 2003. Aftershock sequence of the M_W 7.9 Denali Fault, Alaska, earthquake of 3 November, 2002 from the regional seismic network data. Seismol. Res. Lett. 74, 743–752.
Reed, B.L., Lanphere, M.A., 1974. Offset plutons and history of movement along the McKinley segment of the Denali fault system, Alaska. Geol. Soc. Am. Bull. 85, 1883–1892.
Reznichenko, N.V., Davies, T.R.H., Shulmeister, J., Larsen, S.H., 2012. A new technique for recognizing rock avalanche-sourced deposits in moraines and some palaeoclimatic implications. Geology 40, 319–322.
Richter, D.H., Jones, D.L., 1970. Structure and stratigraphy of eastern Alaska range, Alaska. Am. Assoc. Pet. Geol. Bull. 54, 2502–2512.
Ridgway, K.D., Trop, J.M., Nokleberg, W.J., Davidson, C.M., Eastham, K.R., 2002. Mesozoic and Cenozoic tectonics of the eastern and central Alaska Range: progressive basin development and deformation in a suture zone. Geol. Soc. Am. Bull. 114, 1480–1504.
Rodrìguez, C.E., Bommer, J.J., Chandler, R.J., 1999. Earthquake-triggered landslides: 1980–1997. Soil Dyn. Earthq. Eng. 18, 325–346.
Ruiz, S., Kausel, E., Campos, J., Saragoni, G.R., Madariaga, R., 2011. Identification of high frequency pulses from earthquake asperities along Chilean subduction zone using strong motion. Pure Appl. Geophys. 168, 125–139.
Sappington, J.M., Longshore, K.M., Thompson, D.B., 2007. Quantifying landscape ruggedness for animal habitat analysis: a case study using Bighorn Sheep in the Mojave Desert. J. Wildlf. Manag. 71, 1419–1426.
Sauber, J.M., Molnia, B.F., 2004. Glacier ice mass fluctuations and fault instability in tectonically active Southern Alaska. Earth Planet. Sci. Lett. 42, 279–293.
Schneider, D., Huggel, C., Haeberli, W., Kaitna, R., 2011. Unraveling driving factors for large rock-ice avalanche mobility. Earth Surf. Processes Landf. 36, 1948–1966.
Shugar, D.H., Rabus, B.T., Clague, J.J., Capps, D.M., 2012. The response of Black Rapids Glacier, Alaska, to the Denali earthquake rock avalanches. J. Geophys. Res. 117, F01006.
Shulmeister, J., Davies, T.R., Evans, D.J.A., Hyatt, O.M., Tovar, D.S., 2009. Catastrophic landslides, glacier behaviour and moraine formation – a view from an active plate margin. Quat. Sci. Rev. 28, 1085–1096.
Sosio, R., Crosta, G.B., Chen, J.H., Hungr, O., 2012. Modelling rock avalanches onto glaciers. Quat. Sci. Rev. 47, 23–40.
Stanley, W.D., Labson, V.F., Nokleberg, W.J., csejtey, B., Fisher, M.A., 1990. The Denali fault system and Alaska Range of Alaska: evidence for underplated Mesozoic flysch from magnetotelluric surveys. Geol. Soc. Am. Bull. 102, 160–173.
Stout, J.H., Brady, J.B., Weber, F., Page, R.A., 1973. Evidence for Quaternary movement on Mckinley-Strand of Denali-Fault in Delta-River Area, Alaska. Geol. Soc. Am. Bull. 84, 939–947.
Stout, J.H., Chase, C.G., 1980. Plate kinematics of the Denali fault system. Can. J. Earth Sci. 17, 1527–1537.
Tovar, S.D., Shulmeister, J., Davies, T.R., 2008. Evidence for a landslide origin of New Zealand's Waiho Loop moraine. Nat. Geosci. 1, 524–526.
Uhlmann, M., Korup, O., Huggel, C., Fischer, L., Kargel, J.S., 2013. Supra-glacial deposition and sediment flux of catastrophic rock-slope failure debris, south-central Alaska. Earth Surf. Processes Landf. 38, 675–682.
U.S. Geological Survey, 2002. The 2002 Denali Fault Earthquake Magnitude 7.9 Near Denali National Park, AK. http://earthquake.usgs.gov/earthquakes/eqinthenews/2002/uslbbl/.

Vacco, D.A., Alley, R.B., Pollard, D., 2010. Glacial advance and stagnation caused by rock avalanches. Earth Planet. Sci. Lett. 294, 123–130.

van der Woerd, J., Owen, L.A., Tapponier, P., et al., 2004. Giant, ~M8 earthquake-triggered ice avalanches in the eastern Kunlun Shan, northern Tibet: characteristics, nature and dynamics. Geol. Soc. Am. Bull. 116, 394–406.

van Westen, C.J., Castellanos Abella, E.A., Sekhar, L.K., 2008. Spatial data for landslide susceptibility, hazards and vulnerability assessment: an overview. Eng. Geol. 102, 112–131.

Wilson, F.H., Dover, J.H., Bradley, D.C., Weber, F.R., Bundtzen, T.K., Haeussler, P.J., 2008. Geologic Map of Central (Interior) Alaska. U.S. Geol. Surv. Open-File Rep. OF 98-133-A.

Wolinsky, M.A., Pratson, L.F., 2005. Constraints on landscape evolution from slope histograms. Geology 33, 477–480.

Xu, C., Xu, X., Yu, G., 2013. Landslides triggered by slipping-fault-generated earthquake on a plateau: an example of the 14 April 2010, Ms 7.1, Yushu, China earthquake. Landslides 10, 421–431.